Supporting Information for

Autonomous untethered microinjectors for gastrointestinal delivery of insulin

Arijit Ghosh,[1#] Wangqu Liu,[1#] Ling Li,[2] Gayatri J. Pahapale,[1] Si Young Choi,[1] Liyi Xu,[1] Qi Huang,[1] Ruili Zhang,[1] Zijian Zhong,[1] Florin M. Selaru,[2,3] and David H. Gracias[1,3-8]**

[1]Chemical and Biomolecular Engineering, Johns Hopkins University, Baltimore, MD 21218, USA; [2]Gastroenterology and Hepatology, Department of Medicine, [3]Sidney Kimmel Comprehensive Cancer Center (SKCCC), [4]Department of Oncology, [5]Center for Microphysiological Systems, Johns Hopkins University School of Medicine, Baltimore, MD 21287, USA; [6]Department of Chemistry, [7]Materials Science and Engineering, [8]Laboratory for Computational Sensing and Robotics (LCSR), Johns Hopkins University, Baltimore, MD 21218, USA.

[#] Equal contribution

* Corresponding authors: fselaru1@jhmi.edu; dgracias@jhu.edu

SUPPORTING NOTES

Supporting Note S1: Design of the microinjectors

We designed bidirectional microinjectors with tips that fold in opposite directions to ensure that they can penetrate the gastrointestinal (GI) mucosa, irrespective of the orientation of the injectors. We used two separate and alternating stress layer assemblies in the fabrication process to drive the microinjection tips in opposing directions (Figure S1). The first assembly comprises three injection tips connected by a Y-shaped center. The second assembly includes three other injection tips connected by a hexagonal-shaped center. Compared to designs with two hexagonal-shaped centers, the design that combined a Y-shaped and hexagonal-shaped center significantly reduced microinjector breakage.

We used a multilayer thin-film model by Nikishkov[1] to estimate the desired thickness values of the chromium (Cr) and gold (Au) layers in fabricating the stress layer assemblies. The relevant equations can be found in the reference.[2] In the calculation, we assumed the stress values of Cr to be 1 GPa and that of Au to be zero.[2] We calculated the bending curvature and, by extension, the folding angle of a specific length of the multilayered hinge, which drives the actuation of the microinjection tips. It may be noted that, while in principle, stress layer assemblies having Cr 60 nm/Au 100 nm and Au 100 nm/Cr 60 nm should produce opposing foldable injection tips, we need to add an adhesion-promoting Cr and an Au seed layer for electroplating which required us to incorporate a two-layer and a four-layer assembly to fabricate the microinjectors. We used 15 nm Cr as the first layer to improve the adhesion of the assembly to the Cu sacrificial layer and a 10 nm Au thin film as a seed layer to enhance adhesion and prevent delamination of electroplated films of Ni from the evaporated Cr films. As shown in **Table S1**, we varied the thicknesses for the second stress layer assembly by keeping the first stress layer assembly thicknesses constant at Cr 60 nm/Au 100 nm.

Table S1. Thickness values deposited in the second stress layer for the fabrication of microinjectors from the bottom to the top.

Thickness / Trials	Cr/nm	Au/nm	Cr/nm	Au/nm	Fabrication yield	Predicted folding angle/°
1	10	100	70	5	1.70%	-247.6
2	15	100	75	5	26.10%	-201.1
3	15	100	75	10	99.20%	-176.7

Supporting Note S2: Microinjector safety considerations

We note that the prepared microinjectors consist of gold, nickel, and chromium in their elemental form, which are considered non-toxic. All materials used in this study have been previously widely used in medicine and are generally regarded as inert and stable within the colon.[3-4] For example, Cr in its metal form alloy cobalt-chromium is commonly used in dental and orthopedic implants,[5] Au is widely used in dental implants,[6] and nickel in its metal alloy form of Nitinol (titanium–nickel) for scaffold and stents.[7]

Moreover, we note that Cr, Ni and Au have been widely used in FDA-approved colo-rectal stents such as WallFlex® and Evolution® which are made of Nitinol which contains Ni, Wallstent® is made of stainless steel, which has Cr, and Au is one of the most used radiopaque markers for these colo-rectal stents. [8-11] Also, clinical endoscopic biopsy clips are made of stainless steel with Cr and Au electrodes used for implantable GI devices.[12] The prior use of these metals in biomedical implanted devices mitigates metal toxicity concerns for the microinjectors.

Also, we note that there is a turnover of the GI mucosa every few days,[13-14] and these microinjectors only penetrate the mucosa (see histology data in Fig. 4), so they do not remain or accumulate in the body over the long-term. We have verified their removal in a previously published study with similarly sized devices.[12] Previously, we reported a safety study where 3000 theragrippers (made with the same materials as the microinjectors in this work) were

administrated into the GI tract of live pigs. The pigs showed no sign of gastric obstruction or perforation, ate normally, and showed no evidence of pain or distress. Four weeks after administration of these devices, magnetic resonance imaging (MRI) images of the whole pig GI tract and surgical checking showed that the devices were cleared from the GI tract and there were no more grippers in the animal. These experiments suggest that the grippers are safely eliminated from the body by natural mucosal turnover and are safe for use as microinjectors. To further enhance safety, in the future, alternative materials could also be considered that dissolve in the body and are transient.

Supporting Note S3: Optimization of the thermoresponsive trigger layer deposition

We spin-coated a paraffin wax layer on top of the hinges as the thermoresponsive trigger. The paraffin wax used remains stiff at low temperature and softens at the physiological temperature allowing the injection tip hinges to actuate. However, improper patterning coverage of the paraffin on the hinges (**Figure S2**) results in premature actuation of the tips before it reaches the body temperature inside the GI tract.

We optimized the wax coating conditions for the best wax coverage on the hinges. The distribution of paraffin wax on the wafer is affected by factors such as the wafer's radius, the amount of the viscous liquid, the rotation speed, and rotation time.[15] To achieve optimally uniform wax coverage, we first cut the wafer into quarters to reduce the spinning radius during spin-coating. Next, we spin-coated paraffin wax on microinjectors under different spinning speeds and spinning times, then examined and counted the number of microinjectors with complete wax coverage on the hinges. **Table S2** shows the results of the wax deposition optimization experiments. We obtained optimal results where 96% of microinjectors had relatively uniform coverage on their hinges when 500 μL of paraffin wax was deposited at a spin speed of 500 rpm for 10 s and then 1500 rpm for 40 s.

Table S2. Optimization of wax deposition conditions

Wax volume on each quarters 3" wafer	Step 1		Step 2		The percentage of microinjectors with uniform wax coverage on hinges
	Spining speed	*Time*	*Spining speed*	*Time*	
500 µL	500 rpm	10 s	1000 rpm	10 s	12%
				20 s	13%
				40 s	24%
			1500 rpm	10 s	39%
				20 s	89%
				40 s	96%
			2000 rpm	10 s	51%
				20 s	15%
				40 s	2%

Supporting Note S4: Estimation of the force and pressure exerted by the microinjector tips.

Using maximal force values from the literature, we estimated the force generated by the actuation of the microinjector tips, which measured force during the folding of differentially stressed arms using a force-sensing platform.[16] In that study, a 75 nm Cr/ 115 nm Au stress layer on a 100 µm wide hinge produced a force of 4.7 ± 0.9 µN. Our microinjectors have 60 nm Cr/ 100 nm Au and 100 µm hinges, which should generate a similar force value of around 5 µN.

We used the Hertz contact mechanics model to estimate the pressure exerted by the tip of microinjector arm on the tissue.[14] We approximated the tip of the microinjector as a sphere and the tissue as an elastic half-space. The diameter of the tips was measured from the scanning electron microscope (SEM) images. The microinjectors without a chitosan drug layer have tips of diameter 2R ≈ 3.5 to 5.0 µm. The microinjectors with the chitosan drug layer have tips of diameter 2R ≈ 5.0 to 7.2 µm. We used the value of the microinjector tip's maximum force (F) as 5 µN, according to the literature mentioned above. From the Hertz model, for the contact between a sphere and a half-space, we obtained the maximum pressure applied on the GI mucosa by the injection tip to be, $P_{max} = \frac{1}{\pi}(\frac{6FE^2}{R^2})^{\frac{1}{3}}$, where $\frac{1}{E} = \frac{(1-\nu_{tissue}^2)}{E_{tissue}} + \frac{(1-\nu_{tip}^2)}{E_{tip}}$ was calculated using the Youngs' modulus (E_{tissue} = 0.7 MPa, E_{tip} = 55 GPa) and Poisson's ratio ($\nu_{tissue} \approx 0.4$, ν_{tissue} = 0.42) of the GI mucosa,[17] and the Au injection arm of the microinjector.

Plugging in different injection tip diameters, we found that tips with a chitosan drug patch can apply a pressure of around 0.4 - 0.5 MPa, and the injection tips without a chitosan patch exert a pressure of 0.5 - 0.6 MPa when actuating.

Supporting Note S5: Validation of the enzyme-linked immunosorbent (ELISA) assay.

We conducted initial pilot experiments to ascertain the cross-reactivity of the ELISA assay used for the intrinsic rat insulin and to determine the estimate of the amount of human insulin to be delivered to the rats. We found that the ELISA assay does not react to the intrinsic rat insulin, and a substantial amount of insulin can be detected in the rat plasma when 100 mIU of human insulin was injected via the intravenous route (**Figure S7**). We chose a dose of 60 mIU of insulin in the delivery experiments with microinjectors for an optimal number of 200 microinjectors in each animal.

Supporting Note S6: Microinjector insulin delivery efficiency comparison with other methods

We examined the insulin delivery efficiency of our microinjector and other GI tract-based insulin delivery mechanisms by comparing the maximum insulin plasma concentration and the insulin dosage per body surface area (BSA) of the test animals. We extracted the maximum plasma concentrations and initial dosages from the literature. Then we unified their units to *pM* for the plasma concentration and *mg* for the initial dosage. To calculate the BSA of animals, we assume all rats weigh 0.3 kg (the rats in the literature weigh in the range of 0.25 - 0.3 kg), and all pigs weigh 50 kg (the pigs in the literature weigh in the range of 35 - 65 kg). We calculate the BSA of rats[18] by $BSA = \frac{7.47 \times BW^{\frac{2}{3}}}{100}$, and the BSA of pigs[19] by $BSA = \frac{7.98 \times BW^{\frac{2}{3}}}{100}$, where BW represents the body weight of the animal in the unit of kg.

Supporting Note S7: Theoretical estimation of microinjectors' tissue damage

We measured the histology slides and found that a microinjector arm can cut a line-shaped opening on the mucosa surface, with a size of approximately 200 μm in length and 10 μm in width, corresponding to a surface area of 2×10^{-9} m^2. To theoretically estimate the tissue damage caused by microinjectors, we assume that 3000 microinjectors were administered to a human. Furthermore, we assume that each microinjector makes three incisions in the mucosa since each microinjector has 6 arms folding in two opposite directions. Thus, the total damaged mucosa surface area can be estimated as approximately 1.8×10^{-5} m^2. In contrast, the surface area of the human gut mucosa, which measures 260 - 400 m^2 (approx. tennis court sized), is immense.[20-22] Even in the most conservative estimate of the surface area of the gastrointestinal tract, the microinjectors' damage is at least tens of million-fold smaller relative to the gut mucosa area. These minimal damages are at the cellular level, and we believe they should recover in 1 – 2 days during the natural turnover of the mucosa.

SUPPORTING FIGURES

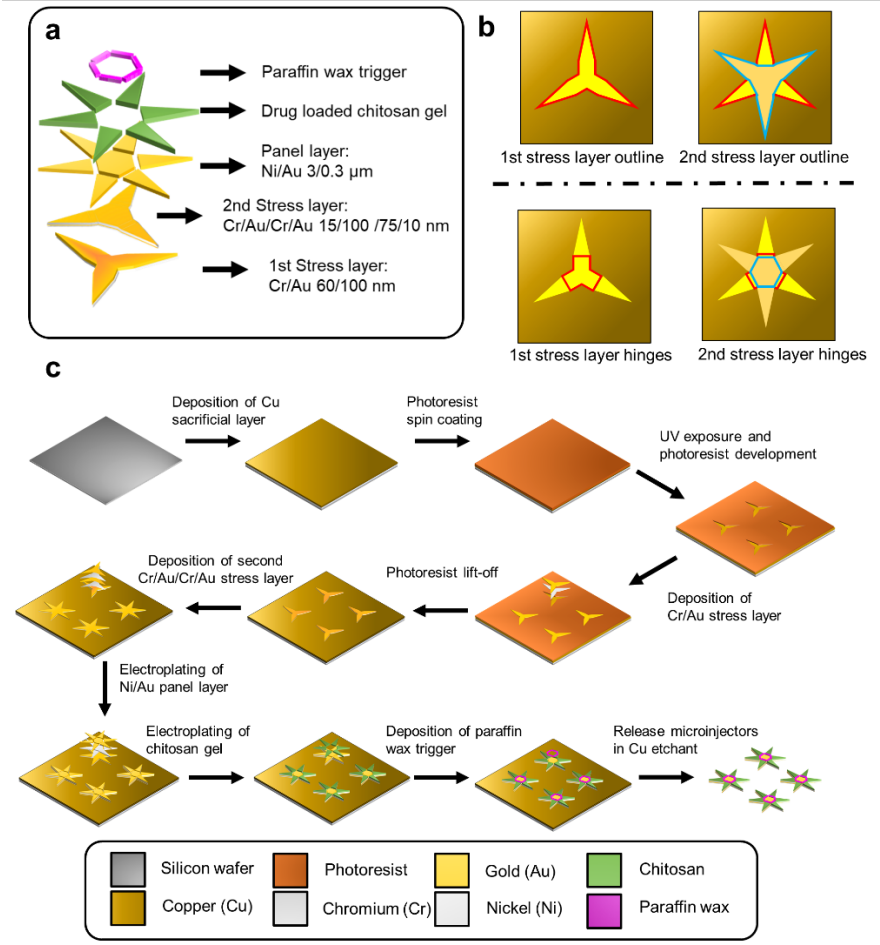

Figure S1: Schematics showing the design and fabrication of the bidirectional foldable microinjectors. (a) Schematic showing the expanded view of the microinjector's five components. From bottom to top, the components are the 1st stress layer, 2nd stress layer, panel layer, drug-loaded chitosan gel, and paraffin wax trigger layer. **(b)** Schematic showing the design of the two stress multilayers. The left panel highlights the outline shape of the differentially stressed multilayers, and the right panel highlights the shape of the differentially stressed multilayers' connections. **(c)** Schematic of step-by-step fabrication of bidirectional foldable microinjectors. The spin coating and UV exposure processes are only shown for the first step, and these processes are repeated for the other patterning steps.

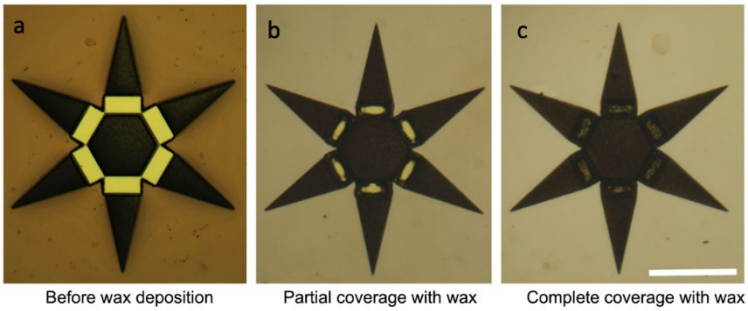

Figure S2: Optimization of the paraffin wax deposition conditions. Bright-field optical microscope images showing, **(a)** the photoresist mold created by lithography on the hinges of the microinjectors, **(b)** partial deposition of paraffin wax due to non-ideal spin coating conditions, and **(c)** complete coverage of the hinge area with paraffin wax using optimized spin coating conditions. The scale bar is 0.5 mm.

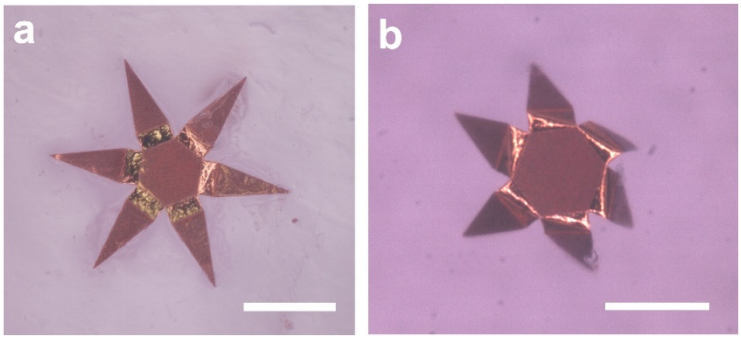

Figure S3: Microinjectors on tissue-mimicking gelatin. Bright-field optical microscope images showing a microinjector, (a) before actuation, and (b) after actuation on 1 kPa stiffness gelatin gel. Note that one-sided microinjectors are shown in these images, where all the injector arms actuate in the same direction. The scale bars are 0.5 mm.

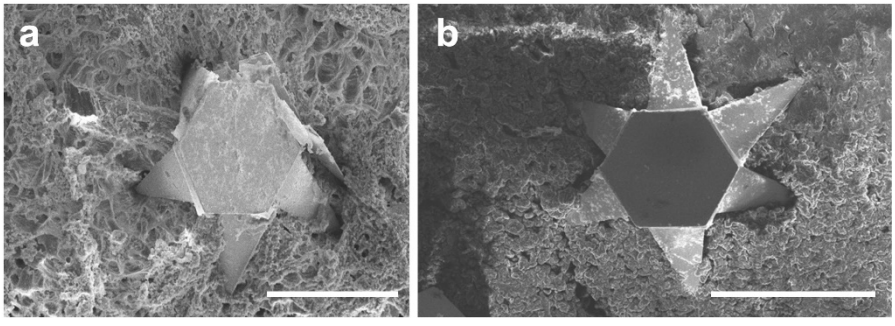

Figure S4: Microinjectors penetrating the pig stomach/colon mucosa. Scanning electron microscope (SEM) images showing results of *ex vivo* experiments in which one-sided microinjectors can successfully penetrate, (a) the pig stomach, and (b) the pig colon mucosa. The scale bars are 0.5 mm.

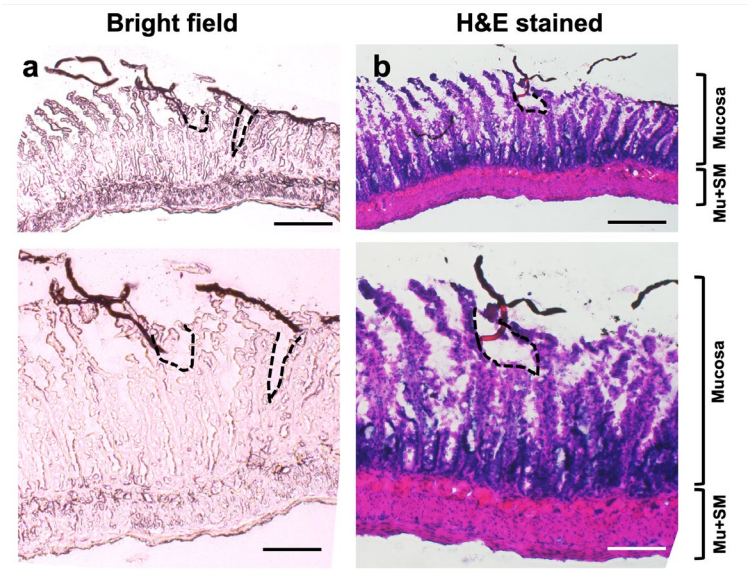

Figure S5: Additional rat colon histology after microinjector actuation. The top panel shows the overview of the tissue slide, and the bottom panel shows the magnification view at the injection site. The scale bars in the top panel are 200 µm, and the scale bars in the bottom panel are 100 µm. (a) Bright-field microscope image of freshly sectioned colon tissue slide at the injection site. Two incisions created by the microinjector arms and the sliced debris of the microinjector arm were observed. (b) Bright-field microscope image of hematoxylin and eosin (H&E) stained colon tissue at the incision site of the microinjector. Mu, muscularis externa; SM, submucosa.

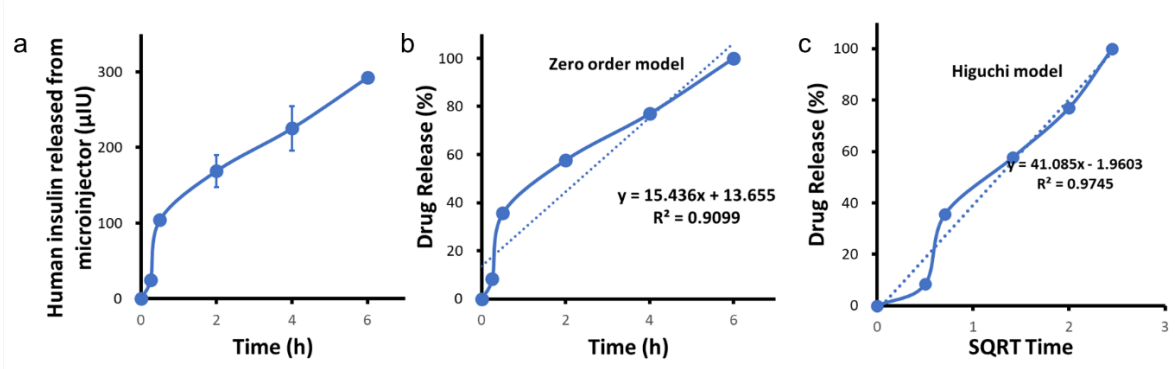

Figure S6: Microinjector *in vitro* drug release profile. (a) Plot showing the cumulative measured amount of human insulin released in saline, normalized by the number of injectors. On average, each microinjector can accommodate around 300 micro IU of human insulin. The *in vitro* release experiments were conducted in an oven, set at 37 °C, and repeated four times to generate the mean and standard error of the mean. Plots showing the measured *in vitro* human insulin release profile fit to, (b) a zero-order kinetics model, and (c) a Higuchi model with an R^2 value of 0.9035 and 0.9745.

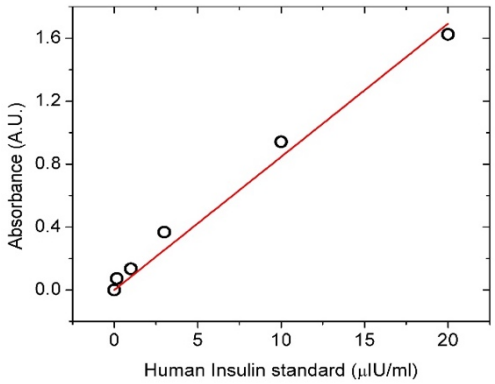

Figure S7: Standard curve showing absorbance vs. insulin concentration at 450 nm. A representative standard curve was obtained using a UV-vis spectrophotometer, showing the linear variation of absorbance at 450 nm as a function of the concentrations of the standard insulin solutions used. The red fit line has an R^2 = 0.9823, indicating a linear response. The standard solutions were obtained from the manufacturer-supplied human insulin ELISA kit.

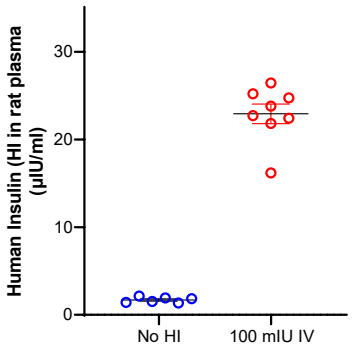

Figure S8: Validation of the non-specificity of the ELISA assay to intrinsic rat insulin. A plot of the measured human insulin concentrations in rat plasma for two conditions: no human insulin administered and 100 mIU human insulin administered intravenously (IV). We collected the blood plasma 30 minutes after the administration of insulin. Points in the plot represent 1 to 3 repeats from the same animal. N = 2 to 4 animals.

SUPPORTING MOVIE

Movie SM1: Video showing thermo-responsive actuation of bidirectional foldable microinjectors sped up 50x.

REFERENCES

[1] G. P. Nikishkov, Curvature Estimation for Multilayer Hinged Structures with Initial Strains. *J. Appl. Phys.* **2003**, *94*, 5333.

[2] T. G. Leong, C. L. Randall, B. R. Benson, N. Bassik, G. M. Stern, D. H. Gracias, Tetherless Thermobiochemically Actuated Microgrippers. *Proc. Natl. Acad. Sci. U. S. A.* **2009**, *106*, 703.

[3] M. Cempel, G. Nikel, Nickel: A Review of Its Sources and Environmental Toxicology. *Pol. J. Environ. Stud.* **2006**, 15(3):375–382

[4] Baruthio, F. Toxic Effects of Chromium and Its Compounds. *Biol. Trace Elem. Res.* **1992**, 32, 145–153.

[5] Mavrogenis, A., Papagelopoulos, P. J., Babis, G. C, Osseointegration of Cobalt-Chrome Alloy Implants. *J. Long-Term Eff. Med. Implants*. **2011**, pp 349–358.

[6] Demann, E. T. K.; Stein, P. S.; Haubenreich, J. E., Gold as an Implant in Medicine and Dentistry. *J. Long Term Eff. Med. Implants* **2005**, *15* (6), 687–698.

[7] Li, J.; Yang, H.; Wang, H.; Ruan, J., Low Elastic Modulus Titanium–nickel Scaffolds for Bone Implants. *Mater. Sci. Eng. C*. **2014**, pp 110–114.

[8] Mangiavillano, B.; Pagano, N.; Arena, M.; Miraglia, S.; Consolo, P.; Iabichino, G.; Virgilio, C.; Luigiano, C. Role of Stenting in Gastrointestinal Benign and Malignant Diseases. *World J. Gastrointest. Endosc.* **2015**, *7* (5), 460–480.

[9] Kim, E. J.; Kim, Y. J. Stents for Colorectal Obstruction: Past, Present, and Future. *World J. Gastroenterol.* **2016**, *22* (2), 842–852.

[10] Chun, H. J.; Kim, E. S.; Hyun, J. J.; Kwon, Y. D.; Keum, B.; Kim, C. D. Gastrointestinal and Biliary Stents. *J. Gastroenterol. Hepatol.* **2010**, *25* (2), 234–243.

[11] Wang, P.-M.; Dubrovsky, G.; Dunn, J. C. Y.; Lo, Y.-K.; Liu, W. A Wireless Implantable System for Facilitating Gastrointestinal Motility. *Micromachines (Basel)* **2019**, *10* (8)

[12] Rees, W. D.; Tandun, R.; Yau, E.; Zachos, N. C.; Steiner, T. S., Regenerative Intestinal Stem Cells Induced by Acute and Chronic Injury: The Saving Grace of the Epithelium? *Front. Cell Dev. Biol.* **2020**, 8, 583919.

[13] Liu, Y.; Chen, Y.-G., Intestinal Epithelial Plasticity and Regeneration via Cell Dedifferentiation. *Cell Regen.* **2020**, 9 (1), 14.

[14] A. Ghosh, L. Li, L. Xu, R. P. Dash, N. Gupta, J. Lam, Q. Jin, V. Akshintala, G. Pahapale, W. Liu, A. Sarkar, R. Rais, D. H. Gracias, F. M. Selaru, Gastrointestinal-Resident, Shape-Changing Microdevices Extend Drug Release In Vivo *Sci. Adv.* **2020**, *6*, 4133.

[15] A. G. Emslie, F. T. Bonner, L. G. Peck, Flow of a Viscous Liquid on a Rotating Disk. *J. Appl. Phys.* **1958**, *29*, 858.

[16] F. Ongaro, Q. Jin, U. Siciliani de Cumis, A. Ghosh, A. Denasi, D. H. Gracias, S. Misra, Force Characterization and Analysis of Thin Film Actuators for Untethered Microdevices.. *AIP Adv.* **2019**, *9*, 055011.

[17] D. C. Stewart, A. Rubiano, M. M. Santisteban, V. Shenoy, Y. Qi, C. J. Pepine, M. K. Raizada, C. S. Simmons, Hypertension-Linked Mechanical Changes of Rat Gut. *Acta Biomater.* **2016**, *45*, 296.

[18] S. L. Diack, The Determination of the Surface Area of the White Rat. *J. Nutr.* **1930**, *3*, 289.

[19] T. Itoh, M. Kawabe, T. Nagase, K. Endo, M. Miyoshi, K. Miyahara, Body Surface Area Measurement in Laboratory Miniature Pigs Using a Computed Tomography Scanner *J. Toxicol. Sci.* **2016**, *41*, 637.

[20] Niess JH, Reinecker HC., Dendritic Cells in the Recognition of Intestinal Microbiota. *Cell Microbiol.* **2006**, 8, 558–64.

[21] Macdonald TT, Monteleone G. Immunity, Inflammation, and Allergy in the Gut. *Science* **2005**, 307, 1920–5.

[22] Helander, H. F.; Fändriks, L. Surface Area of the Digestive Tract - Revisited. *Scand. J. Gastroenterol.* **2014**, *49* (6), 681–689.